

Chapter 8

Density Functional Theory Calculations for Materials with Complex Structures



Ayako Nakata and Yoshitada Morikawa

Abstract Quantum-mechanics-based first-principles density functional theory (DFT) calculations are promising for elucidating the relationship between structures and physical properties at the atomic scale. DFT calculations are highly accurate but conventionally time consuming, which limits the application of DFT to materials having complex structures and reactions affected by many metastable states. To overcome this problem, multi-scale simulations have been conducted using DFT cooperating with statistical methods, such as machine learning techniques, the kinetic Monte Carlo method, and microkinetic modeling. Large-scale calculation methods that reduce the computational cost of DFT have been proposed to treat the complex materials. In this chapter, we summarize the basic concepts of the quantum mechanics calculations (ab initio molecular orbital calculations and first-principles DFT calculations) and then introduce examples of multi-scale calculations using DFT for defects, surfaces, and interfaces and large-scale DFT calculations.

Keywords Density functional theory · Defects · Surfaces · Interfaces · Multi-scale simulation · Kinetic monte carlo simulation · Microkinetic modeling · Large-scale density functional theory

A. Nakata (✉)

Research Center for Materials Nanoarchitectonics (MANA), National Institute for Materials Science (NIMS), Tsukuba 305-0044, Japan

e-mail: NAKATA.Ayako@nims.go.jp

Y. Morikawa

Department of Precision Engineering, Graduate School of Engineering, Osaka University, Suita 565-0871, Japan

e-mail: morikawa@prec.eng.osaka-u.ac.jp

© Materials Research Society, under exclusive license to Springer Nature Singapore Pte Ltd. 2024

K. Hayashi (ed.), *Hyperordered Structures in Materials*, The Materials Research Society Series, https://doi.org/10.1007/978-981-99-5235-9_8

8.1 Quantum Mechanics Calculations

Calculations based on quantum mechanics without using empirical parameters are often called “ab initio” or “first-principles” calculations. In quantum mechanics, electrons are described as either a particle or a wave. De Broglie’s equation expresses the relationship between particle motion and wave motion:

$$\lambda = \frac{h}{p}, \quad (8.1)$$

where p and λ are the momentum and wavelength and h is Planck’s constant. On the basis of Eq. (8.1), Schrödinger’s wave equation, the fundamental equation of quantum mechanics, was derived. The time-independent Schrödinger equation is

$$H\Psi = E\Psi, \quad (8.2)$$

where the operator H is called the Hamiltonian and corresponds to the energy E of the stationary state of the system and Ψ is the wave function containing all the information of the state. Ψ itself is not an observable, but the square of Ψ is an observable.

Once energies of the systems are calculated, energy-related properties such as the formation energy, adsorption energy, and reaction energy can be calculated. Additionally, from the derivative of the energy with respect to the atomic coordinates, the force acting on each atom can be calculated, making it possible to calculate stable structures, transition-state structures, and energies along reaction paths. A molecular dynamics (MD) calculation using these atomic forces is called an ab initio MD (first-principles MD) calculation.

Equation (8.2) expresses a two-body problem and can thus be solved exactly for hydrogen atoms and hydrogen-like atoms (such as He^+ and Li^{2+}) that have one electron and one nucleus but not for atoms larger than He or molecules that contain three or more particles.

In the case of a hydrogen atom, considering that the proton is much heavier than the electron, the nucleus appears to be stationary from the electron’s point of view, and the wave function in polar coordinates is written as

$$\Psi(r, \theta, \varphi) = R_{n,l}(r)Y_{l,m}(\theta, \varphi). \quad (8.3)$$

$R_{n,l}(r)$ is a radial function that represents the spatial distribution of the wave functions. $Y_{l,m}(\theta, \varphi)$ is the spherical harmonic function and represents the directionality of the wave functions. The index n is called the principal quantum number. $n = 1, 2, 3, \dots$ corresponds to the K-shell, L-shell, M-shell. l is called the azimuthal quantum number (or angular momentum quantum number) and m is called the magnetic quantum number. $l = 0, 1, 2, \dots$ corresponds to s-, p-, d-, ... functions, and these functions split according to $m = (-l, -l + 1, \dots, 0, \dots, l - 1, l)$. That is to say, for the

s-function ($l = 0$), $m = 0$; for the p-function ($l = 1$), $m = -1, 0, +1$, corresponding to p_x, p_y, p_z ; for the d-function ($l = 2$), $m = -2, -1, 0, +1, +2$, corresponding to $d_{xy}, d_{yx}, d_{zx}, d_{x^2-y^2}, d_{z^2}$.

8.2 Ab Initio Molecular Orbital Theory

For systems containing three or more particles, Eq. (8.2) cannot be solved exactly, and the goal is thus to obtain an approximate solution that is as accurate as possible [1]. The nucleus is much heavier than the electrons, and the nucleus can thus be approximated as being stationary, which is referred to as the Born–Oppenheimer approximation or adiabatic approximation. Equation (8.2) for electrons then becomes

$$H_{\text{elec}} \Psi_{\text{elec}}(x_1, x_2, \dots, x_{N_{\text{elec}}}) = E_{\text{elec}} \Psi_{\text{elec}}(x_1, x_2, \dots, x_{N_{\text{elec}}}), \quad (8.4)$$

$$H_{\text{elec}} = T + V_{\text{Ne}} + V_{\text{ee}} = \sum_i^{N_{\text{elec}}} \left(-\frac{\hbar}{2m} \nabla_i^2 \right) - \sum_i^{N_{\text{elec}}} \sum_A^{N_{\text{nuc}}} \left(\frac{Z_A e^2}{r_{iA}} \right) + \sum_{i < j}^{N_{\text{elec}}} \left(\frac{e^2}{r_{ij}} \right). \quad (8.5)$$

H_{elec} is the electronic Hamiltonian and Ψ_{elec} is the N -electron wave function. N_{elec} and N_{nuc} are the numbers of electrons and nuclei, respectively. x is a spin coordinate that involves the spatial coordinate \mathbf{r} and spin state s . T , V_{Ne} , and V_{ee} are the kinetic energy, nucleus–electron interaction, and electron–electron interaction terms, respectively. The indices i and A run over electrons and nuclei respectively, and Z_A is the charge of nucleus A . T and V_{Ne} depend on only one electron i , whereas V_{ee} depends on two electrons i and j . When there are three or more electrons, it is difficult to determine the electron–electron interaction exactly because the interaction between two electrons is affected by the other electrons. Therefore, the electron–electron interaction is approximated as the interaction between one electron and the mean field created by the other electrons. This is called the mean-field approximation or one-body approximation. Under this approximation, each wave function corresponds to an electronic state of one electron. This one-electron wavefunction corresponds to what is called the *molecular orbital* (MO) in isolated systems such as molecules and the *band* in periodic systems such as solids.

We need to consider another important quantity of electrons coming from the quantum nature of the electrons, namely the electron spin. In treating electron spin rigorously, we need to consider the relativistic effect. When we simply consider the non-relativistic case, there are two orthogonal spin states, namely α and β spins (also called the up and down spins). The Pauli exclusion principle states that “two electrons cannot occupy the same quantum state (i.e., space and spin) at the same time.” Electrons are fermions, and the electron wave functions are thus anti-symmetric; i.e., the sign of the wave function is inverted when the spaces of two electrons in the same spin state are exchanged. This anti-symmetric behavior can be expressed

using the Slater determinant for wave functions. As a result, the Hartree–Fock (HF) equation is derived as

$$F\psi_i = \varepsilon_i\psi_i, \quad (8.6)$$

$$\begin{aligned} F\psi_i(r_1) = (T + V_{\text{Ne}} + J + K)\psi_i(r_1) = & -\left(\frac{\hbar}{2m}\nabla^2 + \sum_A^{N_{\text{nucleus}}}\left(\frac{Z_A e^2}{r_{iA}}\right)\right)\psi_i(r_1) \\ & + \sum_j^{N_{\text{electrons}}}\langle\psi_j(r_2)|\frac{1}{r_{12}}|\psi_j(r_2)\rangle\psi_i(r_1) - \sum_j^{N_{\text{electrons}}}\langle\psi_j(r_2)|\frac{1}{r_{12}}|\psi_i(r_2)\rangle\psi_j(r_1) \end{aligned} \quad (8.7)$$

The third and fourth terms, J and K , in Eq. (8.7) are Coulomb and exchange interactions, respectively. The exchange integration originates from the Pauli exclusion principle.

In practical calculations, one-electron wave functions are described using basis functions. In calculations of molecules, basis functions in the form of atomic orbitals (AOs) such as s-functions and p-functions are used frequently. The one-electron wave function is approximated as a linear combination of AOs,

$$\psi_i = \sum_{k,\mu} c_{k,\mu}^i \chi_{k,\mu}, \quad (8.8)$$

where $\chi_{k,\mu}$ is μ th AO of atom k and k runs over the atoms in the system. The wave function of a hydrogen atom is a Slater-type function with a cusp at the position of the nucleus. In actual calculations, however, Gaussian functions are widely used because they are easy to integrate. Multiple Gaussian functions with different shapes are combined to reproduce the shapes of AOs. In most cases, the calculation accuracy improves as the number of Gaussian functions increases, although a systematic improvement in accuracy is not guaranteed. In calculations of periodic systems such as solids and surfaces, plane waves are often used as basis functions. In this case, the accuracy of calculations systematically improves as the wave spacing is narrowed (i.e., the wave number is increased). Meanwhile, high-precision plane-wave basis functions often have a considerably higher computational cost than AO basis functions. When plane-wave basis functions are used, the core electrons are not treated explicitly but are often replaced by a function called a pseudopotential. Pseudopotentials are created on the basis of the all-electron calculation of atoms, and the core-electron pseudopotentials are smoothly connected to the potential of the valence electrons treated explicitly using the basis functions. This approach is based on the idea that the change in core electrons from the isolated atom state is small even when atoms are bonded to other atoms. There are several types of pseudopotentials, such as norm-conserving pseudopotentials, ultrasoft pseudopotentials, and projector-augmented waves.

The HF method can describe more than 99% of the total energy of a system, although the electron correlation is roughly approximated by the mean-field approximation. However, actual applications mostly require not the absolute value of the energy of a system but relative energies, which are the differences between the energies of different systems, such as the reaction energy and ionization energy. To discuss these relative energies, a precision of a few kcal/mol (the so-called chemical accuracy) is required in many cases, and the precision of the HF method is often insufficient. The accuracy of the calculation can be improved by including electron correlations more accurately. The energy difference between the exact wave function (E_{exact}) and HF wave function (E_{HF}) corresponds to the electron correlation energy (E_{corr}):

$$E_{\text{corr}} = E_{\text{exact}} - E_{\text{HF}}. \quad (8.9)$$

Several post-HF methods, such as the configuration interaction (CI) method, coupled-cluster (CC) method, and Møller–Plesset (MP) perturbation method, include electron correlation. Figure 8.1 shows that the computational cost of the post-HF methods is much higher than that of the HF method. Full-CI is a method that fully includes electron correlations, and the Full-CI calculation with complete basis functions thus provides the exact energy of the system. However, Full-CI has an enormous computational cost and can only handle very small molecules.

Meanwhile, the density functional theory (DFT) method described in the next section has a computational cost comparable to that of the HF method and is more accurate than the HF method because the DFT method includes electron correlation through exchange–correlation functionals. The DFT method has become the mainstream method for electronic structure calculations because it provides reasonable calculation accuracy at a reasonable calculation cost.

Well-known software packages for quantum mechanical calculations are listed in Table 8.1. Gaussian is commercial software that includes a variety of methods for calculating many types of property. Gaussian is widely used not only by theoreticians but also experimentalists because of its rich interface and user-friendliness. GAMESS is software developed mainly by Iowa State University and available free of charge,

Fig. 8.1 Quantum mechanical calculation methods and their computational costs. The computational cost is shown as the order with respect to the number of atoms N ($O(N^x)$)

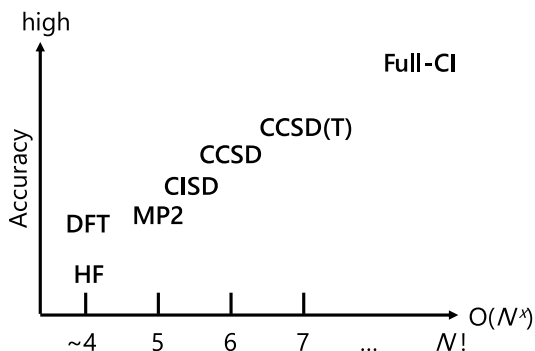


Table 8.1 Software packages for quantum mechanical calculations and their websites

QM software package	website (accessed Jan 2023)
ADF	https://www.scm.com/product/adf/
GAMESS	https://www.msg.chem.iastate.edu/gamess/
Gaussian	https://gaussian.com/
NWChem	https://nwchemgit.github.io/
Q-Chem	https://www.q-chem.com/

and it has a variety of functions. Other software packages, such as ADF, NWChem, and Q-Chem, have been developed with varying performance and functionality.

8.3 Density Functional Theory (DFT)

As mentioned in the previous chapter, the DFT calculation is a highly accurate method that includes electron correlation at a computational cost approximately the same as that of the HF method. DFT is a powerful tool for the investigation of hyperordered structures. DFT describes the electronic state according to the electron density ρ instead of the wave function, considering that the properties of the system are defined by the distribution of electrons [2, 3]. The electron density ρ and N -electron wave function $\Psi(\mathbf{r}, \mathbf{r}_2, \dots, \mathbf{r}_{N_{\text{elec}}})$ have the relationship

$$\rho(\mathbf{r}) = \int ds d\mathbf{r}_2 \cdots d\mathbf{r}_{N_{\text{elec}}} |\Psi(\mathbf{r}_1, \mathbf{r}_2, \dots, \mathbf{r}_{N_{\text{elec}}})|^2, \quad (8.10)$$

$$N = \int \rho(\mathbf{r}) d\mathbf{r}. \quad (8.11)$$

Although the starting points for the DFT and HF methods are different, the basic equation of DFT, the Kohn–Sham equation, [4] has a form similar to that of the HF equation. Below, we look at the DFT method in more detail.

The fundamental theorem of DFT, the Hohenberg–Kohn theorem, [5] and Levy’s constrained search [6] guarantee a one-to-one correspondence between the electron density and the external potential $v(\mathbf{r})$ and the variational principle of the DFT total energy. ρ is a function of the coordinate \mathbf{r} , and the energy E of the system in DFT is thus a functional of ρ written as $E[\rho]$. When the interaction with the nucleus is treated as an external field $v(\mathbf{r})$, $E[\rho]$ is written as

$$E[\rho] = E_{\text{T}}[\rho] + E_{\text{Nc}}[\rho] + E_{\text{ee}}[\rho] = E_{\text{T}}[\rho] + \int \rho(\mathbf{r})v(\mathbf{r})d\mathbf{r} + E_{\text{ee}}[\rho]. \quad (8.12)$$

E_T and E_{ee} are the kinetic and electron interaction energies, where $E[\rho]$ corresponds to the exact energy including electron correlations in the N -electron system.

Kohn and Sham introduced the concept of one-electron orbitals [4] into DFT. Using the Kohn–Sham (KS) orbitals, Eq. (8.10) is rewritten as

$$\rho(\mathbf{r}) = \sum_i f_i |\varphi_i(\mathbf{r})|^2, \quad (8.13)$$

where f_i is the occupation number of the i -th KS orbital. When E_T^{KS} is the kinetic energy calculated using the KS orbitals rather than the electron density, the exchange–correlation energy E_{xc} can be written by separating the kinetic energy E_T^{KS} and Coulomb repulsion energy $J[\rho]$ from $E_T[\rho]$ and $E_{ee}[\rho]$ in Eq. (8.12):

$$E_{xc}[\rho] = E_T[\rho] - E_T^{\text{KS}} + E_{ee}[\rho] - J[\rho]. \quad (8.14)$$

E_{xc} is the non-classical term obtained by subtracting the classical term from $E[\rho]$ and includes corrections for both E_T^{KS} and E_{ee} . Given that the Euler equation for Eq. (8.12) is solved using Lagrange’s method of undetermined multipliers, the KS equation is written as

$$\begin{aligned} F\varphi_i(\mathbf{r}) &= (T + V_{\text{Ne}} + J + V_{\text{xc}})\varphi_i(\mathbf{r}) \\ &= \left[-\frac{\hbar}{2m}\nabla^2 + v(\mathbf{r}) + \int \frac{\rho(\mathbf{r}')}{|\mathbf{r} - \mathbf{r}'|} dr' + \frac{\delta E_{xc}[\rho]}{\delta \rho(\mathbf{r})} \right] \varphi_i(\mathbf{r}) \\ &= \varepsilon_i \varphi_i(\mathbf{r}). \end{aligned} \quad (8.15)$$

ρ is updated as in Eq. (8.13) depending on φ updated as in Eq. (8.15) should thus be solved self-consistently. This KS equation has the same form as the HF equation, Eq. (8.7), except that the KS equation contains E_{xc} instead of the exchange energy K that is included in the HF equation. In other words, the many-electron correlation is put into E_{xc} , and Eq. (8.15) itself is reduced to the one-electron problem. Thus, the KS equation can be solved with the same computational order as the HF equation, while the electron correlation is considered via E_{xc} .

Compared with the HF method, which is based on an approximate theory that fundamentally lacks electron correlation, the KS method obtains exact energies without approximation if the exact form of E_{xc} is known. However, because the exact E_{xc} is unknown at present, an approximate exchange–correlation functional must be used in actual calculations. Therefore, the accuracy of DFT calculations depends on the exchange–correlation functional used.

The exchange–correlation functional can be divided into two parts: the exchange part and correlation part. Various types of exchange–correlation functional have been proposed according to two fundamental requirements, namely the adequacy of the description of fundamental physical properties (e.g., a description of exchange–correlation holes) and the accurate reproduction of physical quantities (e.g., the reproduction of molecular structures and reaction energies). The most basic exchange–correlation functional is the local density approximation (LDA), which assumes a

uniform electron gas with density ρ . Although the LDA is a crude approximation that expresses the exchange–correlation functional in terms of density $\rho(\mathbf{r})$ alone, it is often accurate enough for the calculation of the electronic structures of solids and has often been used successfully. However, there remain several problems; for example, the cohesive energy of solids cannot be calculated with high accuracy, and physical quantities cannot be described with chemical precision in molecular calculations. Therefore, the generalized gradient approximation (GGA) functional, which improves on the LDA functional by adopting the density gradient $\nabla\rho$, was developed. GGA functionals such as PBE [7] and PBEsol [8] are now the mainstay of calculations for solids. Although the use of the GGA has improved the accuracy of calculations, there remain problems, such as the underestimation of the band gap of semiconductors and insulators and the inability to represent dispersion forces.

Therefore, meta-GGA and hybrid functionals have been developed to further improve the GGA. Meta-GGA is a correction of the GGA functional made using the second derivative of density $\nabla^2\rho$ and kinetic energy density τ [9–11]. The hybrid functional corrects the GGA exchange functional by adopting the HF exact exchange term. (In contrast to the hybrid functional, the functional without the correction with the HF exchange term is often called the pure functional.) One of the most widely used hybrid functionals is the B3LYP functional, [12] which is a combination of Becke’s three-parameter (B3) hybrid exchange functional and Lee–Yang–Parr’s correlation functional. In the HF method, the unphysical self-interaction (i.e., the interaction when the indices i and j in Eq. (8.7) are the same) disappears completely through J and K , canceling each other out. In contrast, in DFT using the pure functional, the self-interaction remains because the exchange functional is not exact. This self-interaction error can be reduced by mixing the HF exact exchange term in the hybrid functional. Range-separated functionals [13–15] allow the use of different proportions of the HF exact exchange for long- and short-range interactions. Meta-GGA and hybrid functionals thus dramatically improve the accuracy of bandgap calculations.

The use of the DFT + U method improves the accuracy of the description of 3d and 4f electrons, which are highly localized and have strong electron correlations. In this method, the orbital energy levels are artificially adjusted by correcting Coulomb interactions in the form of the Hubbard model with the parameter U. Although it is a somewhat empirical method, it improves the accuracy of calculations for 3d transition metal oxides, such as TiO₂, when the U parameter is set appropriately.

The calculations of dispersion forces have been improved using the van der Waals (vdW)-density functional (DF) [16, 17] and DFT with dispersion correction (DFT-D) [18] methods, which incorporate long-range electron correlations approximately. These methods enable accurate calculations for organic solids and physically adsorbed systems. For example, the calculation of the graphite interlayer distance has been much improved using the vdW-DF method [19].

A further way to improve the exchange–correlation functional is to consider the effect of unoccupied orbitals. Improvements in the accuracy of the functional are still being widely made and are approaching a universal functional. Perdew’s Jacob’s ladder [20] succinctly describes this stepwise improvement of the functional

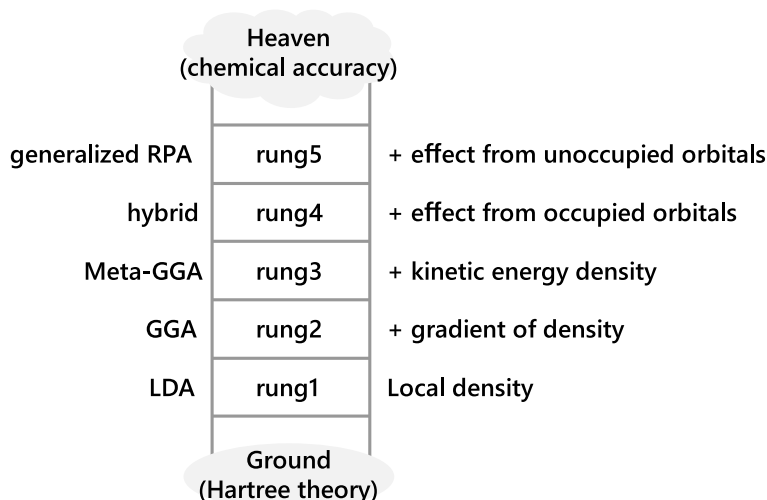


Fig. 8.2 Jacob's ladder for the improvement of density functionals [20]

(Fig. 8.2). Additionally, the use of machine learning to improve the accuracy of DFT calculations has been proposed recently.

DFT fits well with calculations using periodic boundary conditions such that is widely used for solid and surface calculations. Additionally, the DFT method is now the mainstream method for molecules as well, because it has the same or better accuracy at a lower computational cost relative to the MP2 method (see Sect. 8.2), which has conventionally been used for chemical reaction calculations. Meanwhile, it is noted that the improvement in the accuracy of the exchange–correlation functionals in DFT calculations is not as systematic as that for the post-HF methods. It is necessary to use functional and correction methods that are appropriate for the calculation target. Some of the often-used DFT calculation programs for solid-state physics are given in Table 8.2, and many other solid-state physics DFT calculation programs exist. The DFT method is also implemented in the quantum chemistry calculation programs given in Table 8.1.

Table 8.2 DFT codes used in solid-state physics

DFT software	website (accessed Jan 2023)
CASTEP	http://www.castep.org/
PHASE	https://azuma.nims.go.jp/
QUANTUM ESPRESSO	http://www.quantum-espresso.org/
STATE-Senri	https://state-doc.readthedocs.io/en/latest/index.html
VASP	https://www.vasp.at/

8.4 Application of DFT to Defects, Surfaces, and Interfaces

In this section, several applications of DFT to defects, surfaces, and interfaces are presented. Solid surfaces and interfaces, as well as impurities and defects in solids, play a major role in determining device functions and performance. Therefore, in constructing devices that are more efficient, it is important to clarify the correlations between the structures and functions of surfaces/interfaces, impurities, and defects, and to control them. However, because solid surfaces, interfaces, and defects do not have translational symmetry and are usually complex structures, it is often difficult to clarify the atomic structure only by experiment. In the field of hyperordered structure science, attempts are being made to experimentally clarify solid surfaces, interfaces, and defect structures. However, it remains difficult to determine the structure clearly only by experiment. Therefore, highly reliable and computationally efficient first-principles electronic structure simulation methods play important roles [21, 22].

Heterogeneous catalysts play important roles in various fields relating to material synthesis, energy, and environmental problems. Heterogeneous catalytic reactions do not necessarily occur on a stable flat solid surface but rather steps, kink sites, and more complex so-called active sites that have formed on a small part of the solid surfaces, where most of the catalytic reactions take place. The clarification of these special active sites is a target of hyperordered structure science.

First-principles electronic structure calculation methods based on DFT have become widely used, and the chemical reactivity of various solid surface structures such as flat surfaces, steps, kink sites, and nanoclusters has been investigated.

To truly understand the catalytic reaction mechanism, we need to investigate thermodynamically metastable but catalytically highly active sites for non-equilibrium conditions under which chemical reactions are proceeding. To this end, multi-scale simulation techniques involving first-principles calculations and statistical methods such as machine learning techniques, kinetic Monte Carlo (KMC) simulation, and microkinetic modeling are indispensable.

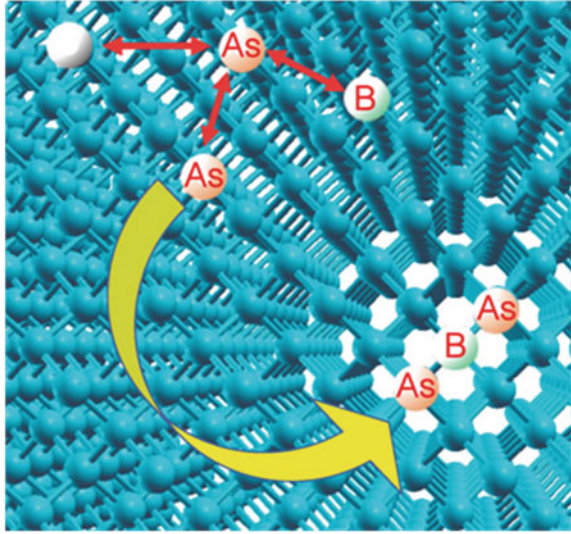
This section provides an overview of the status of these research topics.

8.4.1 *As and B Co-Doped Si*

Controlling the formation of impurity clusters is important when doping a semiconductor with impurities at a high concentration. Through photoelectron holography combined with first-principles simulations, we reported that some of the inactivated As atoms form a cluster structure called As_nV ($n = 2$ to 4) for As doped in Si [23]. This structure is one in which two to four As atoms occupy the nearest neighboring sites around the Si vacancy.

Meanwhile, we theoretically predicted that replacing the vacancies of the above cluster structure with B atoms in the process would stabilize the structure and activate the electrically inactive As atoms (Fig. 8.3) [21, 22]. This suggests the possibility of

Fig. 8.3 As and B dopants become stable by forming a cluster in contrast with isolated individual dopants



developing a new processing technology that further increases the upper limit of the active As concentration. Even if B itself is activated as an acceptor to compensate for the donor of As, the electron carrier concentration can be increased if 2–4 atoms of As per B atom can be doped (Fig. 8.4).

We show the density of states for (a) pristine Si crystal, (b) As-doped Si crystal, and (c) an As_2V cluster in Si crystal in Fig. 8.4. Two-way arrows indicate the band gap of the host Si crystal. If an As atom replaces a Si atom in the Si crystal, one extra electron is donated into the conduction band, leading to the shift of the Fermi level from the middle of the band gap to the bottom of the conduction band (Fig. 8.4b). In contrast, if two As atoms are located at the second nearest neighbor sites and are separated by one Si vacancy, forming an As_2V cluster, then a mid-gap state appears in the band gap, causing electron or hole trapping, clearly indicating the inactive nature of the cluster (Fig. 8.4c). To suppress the mid-gap states, we propose forming a complex of dopants, namely two As dopants with one B dopant, forming an As_2B cluster. By forming a composite cluster of As and B, the mid-gap state disappears and the Fermi level is positioned at the bottom of the conduction band (Fig. 8.4d), clearly showing that the As_2B complex cluster acts as an n-type dopant. Therefore, we propose co-doping As and B in a Si crystal at a ratio of 2:1 to form a highly doped n-type semiconductor. We then predict that active As_2B complex clusters will form and As_nV type inactive clusters are suppressed even under heavy doping conditions.

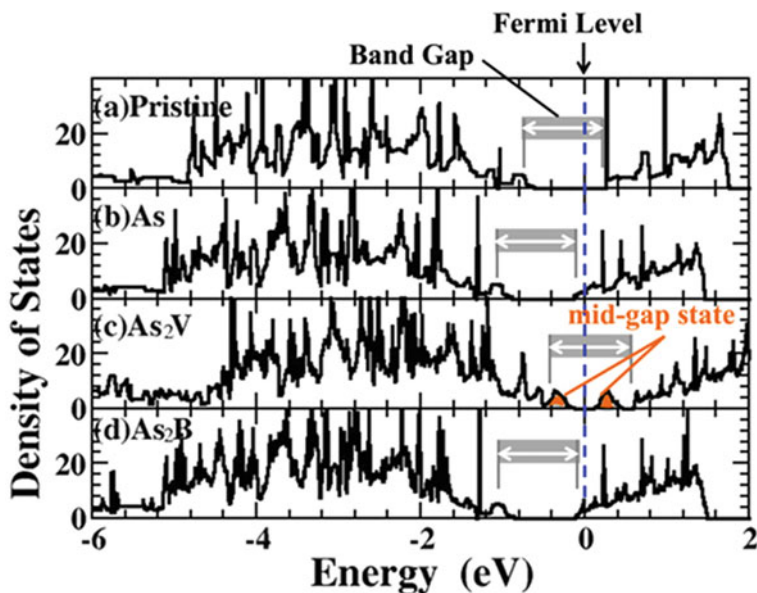


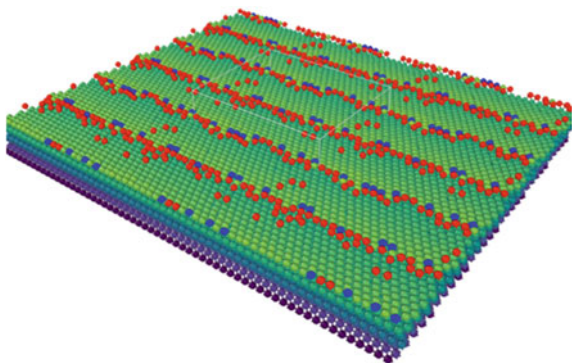
Fig. 8.4 Density of states of **a** pristine Si, **b** Si doped with a single As atom, **c** a cluster of two As atoms and V, and **d** Si co-doped with As and B. Reproduced with permission from Ref. [22]

8.4.2 *Cu–Zn Surface Alloying on Cu(997) Using the Machine Learning Potential*

Catalysts based on metal alloys are well recognized in the world of heterogeneous catalysis given that they have unique properties when alloyed. Given the optimal composition and environment, these catalysts can outperform their alloy constituents in terms of catalytic performance.

In heterogeneous catalysis, metal alloys are known to have highly specific reactivities compared with simple metals. Reactivity varies greatly with alloy composition, so predicting how reactions will change with alloying is important to catalyst design. There are various examples of the application of metal-alloy-based catalysts in heterogeneous catalysis. Methanol is synthesized from gas mixtures of H_2 , CO, and CO_2 using Cu/ZnO/ Al_2O_3 (CZA) catalyst, and isotope experiments showed that the C source of methanol is CO_2 rather than CO. Furthermore, it has been reported that Cu–Zn surface alloy is active for methanol synthesis from CO_2 and H_2 . Experiments combining surface science and powder catalyst have been carried out, with the reactivity and activation energy of methanol synthesis on the Zn-deposited Cu(111) surface being in good agreement with the results for powder catalysts, indicating that a Zn-deposited Cu surface is a good model catalyst of CZA. Further experiments have investigated the reactivity of methanol synthesis on Zn-deposited Cu(111) surfaces, finding that the activity increased in proportion to the Zn coverage up to 0.19 ML.

Fig. 8.5 Bird-eye’s view of the Cu(997) slab model, which has six layers and comprises 2352 atoms with two step edges and 20 atoms in each row per unit cell



In this study, to understand the formation process of catalytically active Cu–Zn alloys at the atomic level, we constructed a machine learning potential from the data of the first-principles electronic structure calculation and used the potential in long-time molecular dynamics simulations [24]. The MD simulations were carried out using a force field trained by Gaussian process (GP) regression, which utilizes the uncertainty information of predicted forces and enables an active on-the-fly learning scheme for building the force field efficiently. The database, containing information on atomic forces acting on various environments, was obtained from DFT calculations. We used a program called “Fast Learning of Atomistic Rare Events (FLARE)” to construct a GP force field [25].

We used a Cu(997) surface model that consists of 2352 atoms with two step edges and 20 atoms in each row per unit cell (Fig. 8.5).

To investigate the alloying process, we performed a molecular dynamics simulation with an NVT ensemble at 700 K for up to 6.25 μs . Figure 8.6 shows the time evolution of Zn atoms on Cu(997) until the Cu–Zn surface alloy forms. To clearly show the distribution of Zn atoms substituted on the surface Cu atoms, the distribution of substituted Zn atoms in each row when viewing the surface from the side is also shown in the figure. Such plots accompany each MD snapshot in Fig. 8.6.

Initially (Fig. 8.6a), the Zn atoms are localized at the step edge and cover the Cu steps. After 1.25 μs , some Zn atoms are attached at the upper and lower terraces near the step edges (Fig. 8.6b). It is seen that many Zn atoms are accommodated on the upper terraces, whereas few atoms are accommodated on the lower terraces.

Zn is incorporated into the subsurface layer, such as at 1.25 μs (Fig. 8.6b) and 3.75 μs (Fig. 8.6d). At 6.25 μs , we finally find Zn atoms on the middle terrace (Fig. 8.6f). The trend observed in this simulation suggests that the alloying initiates on the upper and lower terraces near the step edges, and Zn atoms are found later on the middle terrace.

Our simulation reveals details of the alloying process at the atomic scale; i.e., the incorporation of Zn adatoms to the Cu substrate from the step edges. We found Zn atoms not only on the upper terrace but also on the lower and middle terraces near the step edges, which has not been considered in previous DFT studies on methanol

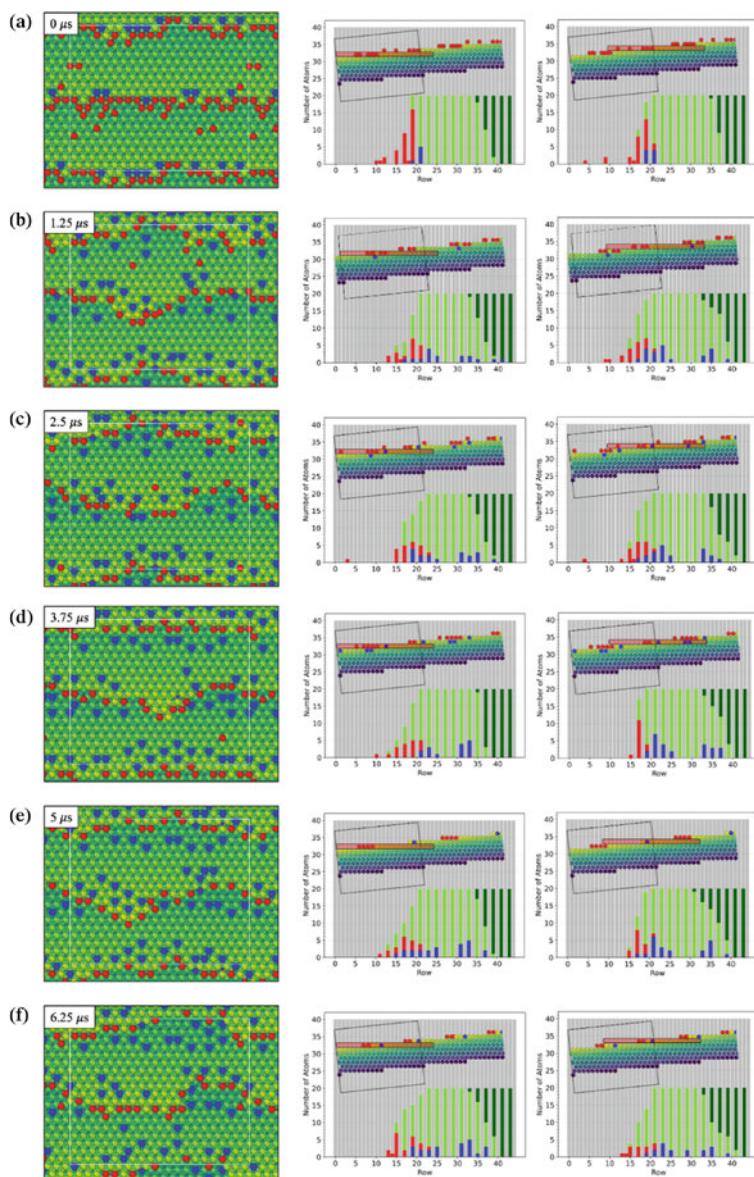


Fig. 8.6 Top and side snapshots of MD simulations for Zn-deposited Cu(997) surfaces. The green to yellow spheres indicate Cu atoms, the red spheres indicate Zn adatoms, and the blue spheres indicate substituted Zn atoms. The distribution of adatoms and substituted Zn atoms in each row is also shown. In each plot, the red, blue, light green, and dark green bars indicate the number of Zn adatoms, Zn incorporated atoms, Cu surface atoms, and Cu atoms covered by the additional Zn layer. Reproduced from Ref. [24]. CC-BY 4.0

synthesis on a Cu–Zn surface. We also found that all the elementary events involving Zn atoms have a lower barrier than the pure Cu system, suggesting Zn atoms enhance the step edge fluctuations.

The time evolution of the surface structure reveals that alloying occurs near the step edges. In addition, a detailed energy analysis reveals that the activation energy barrier for an atom to pop-out or kick-out another atom is much lower near the step edges than on a flat terrace. Furthermore, alloyed Zn atoms are observed near the center of the terrace as time passes. It was found that the formation of alloyed Zn near the center of these terraces is related to the steps. Initially, alloyed Zn forms near the step, and the location of the step then sways away, leaving the alloyed Zn at the center of the terrace.

8.4.3 *Equilibrium Step Fluctuations on the Cu(111) Surface Using Kinetic Monte Carlo Simulation*

The molecular dynamics method based on the machine learning potential is epoch making in that it greatly extends the time and space scales while maintaining the computational accuracy at the level of the first principles simulations. However, the time scale is still limited to the μs order. The kinetic Monte Carlo (KMC) method is effective for studying longer phenomena on the order of seconds. Here, we introduce a recent study on step fluctuations on the Cu(111) surface using the KMC method [26].

We study the diffusion of Cu adatoms on the Cu(111) surface using DFT-KMC simulation tools. There are two main reasons why we begin with this model. First, the investigation on Cu surfaces can be considered as a prerequisite in the elucidation of active sites of the industrial catalyst Cu/ZnO/Al₂O₃. Second, the homoepitaxial growth of Cu has been well investigated in a large number of theoretical and experimental studies [27–32]. One important topic of study is the time correlation function, from which the dominant atomic diffusion process can be identified. Therefore, in this work, we conduct a DFT-KMC simulation adopting cluster expansion (CE) to elucidate the microscopic mechanism of the surface diffusion of Cu, especially with defects such as steps and kinks.

The CE method describes the total energy of a system as the sum of the effective cluster interactions of small clusters such as two-body, three-body, and tetra-body interactions. The Hamiltonian of the system or the total energy of a lattice configuration, denoted as $H(\sigma)$, is given by

$$H(\sigma) = \sum_{k=1}^{N_c} \frac{ECI_k}{GM_k} NCE_k(\sigma), \quad (8.16)$$

where E_{CI_k} is the effective cluster interaction of cluster k , GM_k is the graph multiplicity of cluster k , and NCE_k is the number of detected clusters k in the current configuration. There are 48 clusters, including fcc, hcp, and fcc-hcp clusters.

The activation energy barrier of each process is described using the Brønsted–Evans–Polanyi principle from the initial and final state energies of each process:

$$E_{act}^{fwd}(\sigma) = \max(0, \Delta E(\sigma), E_{act}^{fwd,0}(\sigma) + \omega \cdot (\Delta E(\sigma) - \Delta E^0(\sigma))), \quad (8.17)$$

$$E_{act}^{rev}(\sigma) = \max(-\Delta E(\sigma), 0, E_{act}^{rev,0}(\sigma) - (1 - \omega) \cdot (\Delta E(\sigma) - \Delta E^0(\sigma))), \quad (8.18)$$

where E_{act}^{fwd} and E_{act}^{rev} are respectively the activation energy barriers for the forward and reverse reactions, and ΔE is the reaction energy, which is the energy difference between the final and initial states of the reaction. The superscript “0” for the reaction energy and activation energy barriers indicates the limit at zero coverage. These energies were obtained by calculation with low coverage of adatoms on the Cu(111) surface using DFT. ω is the *proximity factor* of the transition state relative to the final state of the reaction, ranging from 0 to 1.

We performed KMC simulation using a graph-theoretical framework, as implemented in Zacros developed by Stamatakis et al. [33]. As the elementary process, we adopted reversible hopping from the fcc hollow site of the adatom to the hcp hollow site. We used an approximate pre-exponential factor of 10^{12} s^{-1} as suggested by previous studies. We used a surface model of 42×42 unit cells having fcc and hcp lattice sites to capture the stable structure of the adatoms. A periodic boundary condition was imposed for both x and y axes.

This type of model has four important parts. Step A comprises the (100) facet whereas step B comprises the (111) facet, kink sites, and the flat terrace of Cu(111). We confirmed that the number of rows between the two steps was sufficient to avoid the mutual interaction of the steps. We first performed the equilibration of the surface structure by conducting the KMC simulation (shown schematically in Fig. 8.7) for a certain length of time until no significant change in the step structure or energy was detected.

To confirm the reliability of our CE, we compared the reaction and activation energies of various diffusion events at step A estimated from CE with direct DFT calculations. The activation energies are presented in Fig. 8.8. Our calculations show that the reaction energies obtained from CE and DFT are in good agreement with each other, with the difference being no more than 0.10 eV. The discrepancy between the CE and DFT is attributed to the limited size of the clusters that we used and the effect of atomic relaxation from DFT calculations.

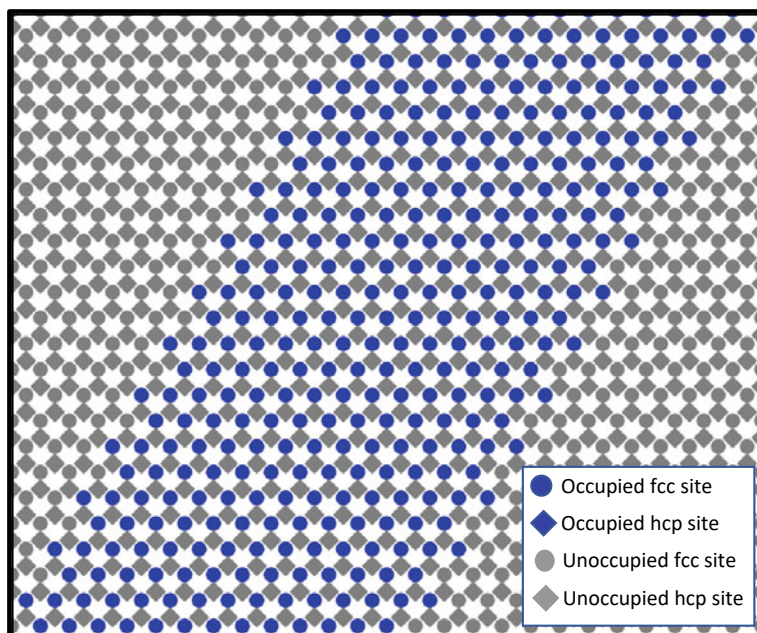


Fig. 8.7 Starting configuration in our KMC simulation. Blue circles and diamonds represent the occupied fcc and hcp sites, respectively. Grey circles and diamonds represent the unoccupied fcc and hcp sites, respectively. Reproduced from Ref. [26]. CC-BY 4.0

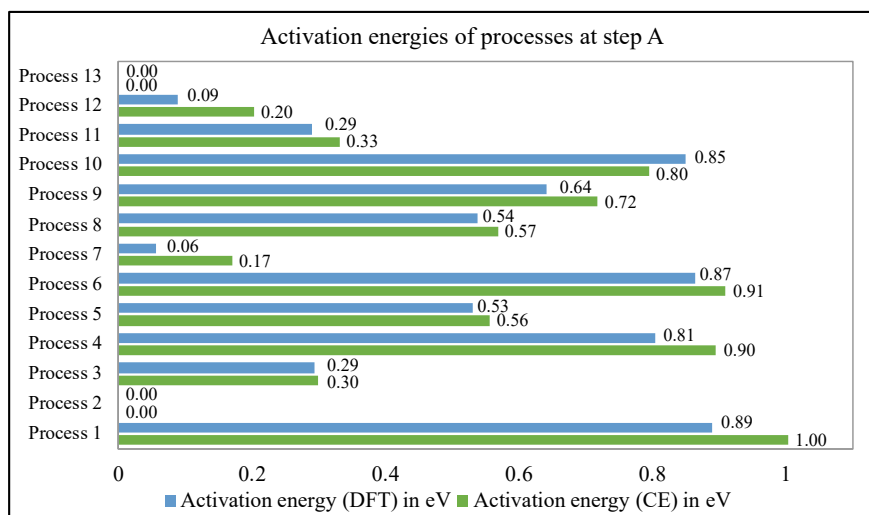


Fig. 8.8 Activation energies for various processes obtained from direct DFT calculations (blue bars) and the CE framework (green bars) for step A. Reproduced from Ref. [26]. CC-BY 4.0

8.4.4 Formic Acid Adsorption and Decomposition on Cu(111) in Micro-Kinetic Analysis

The KMC simulations combined with the first-principles electronic structure calculation method are limited to a time-scale order of seconds. Micro-kinetic modeling, which treats the reaction rate as a function of concentration in a mean-field manner, is effective for examining reactivity over a longer time scale. Micro-kinetic modeling has often been combined with first-principles simulations to predict the reactivity of heterogeneous catalysis. Here, we introduce recent work on formic acid adsorption and decomposition on Cu(111) [34].

In recent years, how to store hydrogen safely and efficiently has become an issue for the realization of a hydrogen society. Formic acid is attracting attention as a candidate solution. Formic acid will be useful as a hydrogen carrier if it can be decomposed into hydrogen molecules and carbon dioxide with high selectivity and efficiency. Therefore, the development of an efficient and highly selective catalyst for formic acid decomposition is desired. We investigated the adsorption and decomposition processes of single HCOOH on Cu(111) using DFT calculations including vdW forces and compared them with the results of room-temperature experiments.

Next, the kinetic analysis of the desorption and decomposition reaction processes of formic acid was carried out. Activation energy barriers and pre-exponential factors were estimated from the results of first-principles electronic structure calculations. The desorption rate was derived from the detailed balance condition of the adsorption and desorption rates, assuming that the surface adsorbates are in equilibrium with the gas-phase formic acid at temperature T and pressure P . The rate of desorption can be expressed by the flux (F) of impinging molecules on the surface per unit area and unit time, multiplied by the sticking probability $S(\theta, T)$,

$$r_{\text{des}} = r_{\text{ads}} = FS(\theta, T) = \frac{P_{\text{eq.}}}{\sqrt{2\pi mk_{\text{B}}T}} S(\theta, T), \quad (8.19)$$

where $P_{\text{eq.}}$, m , k_{B} , and T are equilibrium pressure, molar mass of the molecule, Boltzmann's constant, and temperature of the system, respectively.

We calculate the decomposition rate using Eyring's transition state theory with the assumption that the activated complexes are in equilibrium with the reactants. Thus, the kinetic constant for the decomposition, which corresponds to the decomposition rate per surface adsorbate, is expressed as

$$k_{\text{dec}} = \frac{r_{\text{dec}}}{n_s \theta} = \frac{k_{\text{B}}T}{h} \frac{Q_{\text{TS.}}}{Q_{\text{ads.}}} \exp\left(-\frac{E_{\text{dec}}}{k_{\text{B}}T}\right), \quad (8.20)$$

where E_{dec} is the difference in energy between the transition state and the HCOOH adsorbed on the surface ($E_{\text{dec}} = E_{\text{TS.}} - E_{\text{ads.}}$). $Q_{\text{TS.}}$ and $Q_{\text{ads.}}$ are the products of partition functions of the translational, rotational, and vibrational degrees of freedom for the transition state and adsorbed phase, respectively.

The reaction path and activation energies for the decomposition (E_{dec}) of the OH-perpendicular configuration on the Cu(111) surface are shown in Fig. 8.9. We conclude that the decomposition starting from the OH-perpendicular configuration to the bidentate HCOO is the most dominant path among the three decomposition paths considered and accordingly, in the decomposition rate analysis, we focused on the decomposition path from the OH-perpendicular configuration to bidentate HCOO on the Cu(111) surface.

On the basis of vdW energy functionals, the desorption energy is greater than the activation energy barrier for the decomposition of HCOOH. At first glance, this seems to indicate that decomposition dominates desorption, which is inconsistent with the experimental result that no formic acid decomposition was observed on the Cu(111) surface when the surface was exposed to gas-phase HCOOH at room temperature whereas the decomposition was observed when the surface was exposed to the gas-phase HCOOH at low temperatures and heated to approximately 188 K [35–41]. This seemingly contradictory result can be resolved by calculating the reaction rate from first-principles calculations. In other words, the pre-exponential factor for desorption is much larger than the pre-exponential factor for decomposition, such

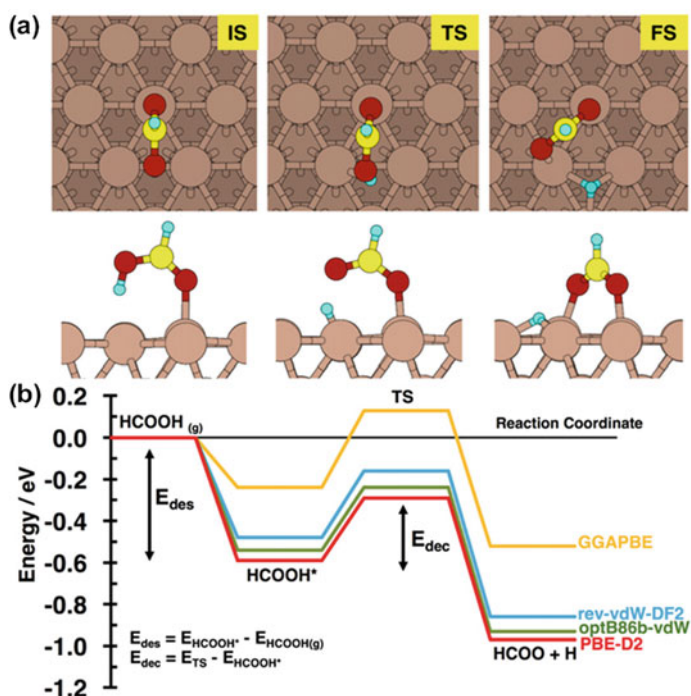


Fig. 8.9 **a** Decomposition of the OH-perpendicular configuration. IS, TS, and FS represent the initial state, transition state, and final state, respectively. **b** Energy profile for the OH-perpendicular configuration decomposition on Cu(111). The energy zero is taken as the energy of the gas-phase HCOOH (HCOOH(g)). Reproduced from Ref. [34]. CC-BY 4.0

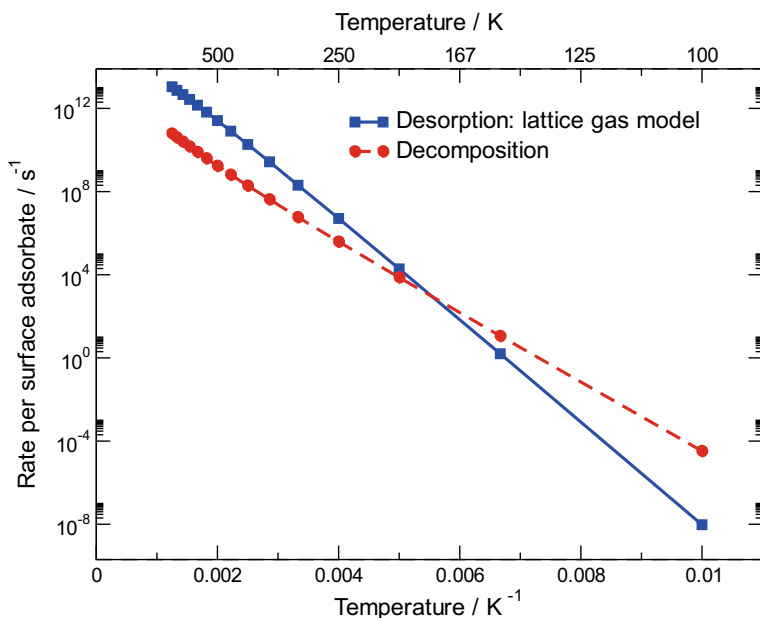


Fig. 8.10 Calculated reaction rates per surface adsorbate for the desorption and decomposition of the OH-perpendicular configuration. The red dashed line with circles and blue solid line with squares respectively represent the decomposition and desorption rates obtained using the two-dimensional lattice gas. Reproduced from Ref. [34]. CC-BY 4.0

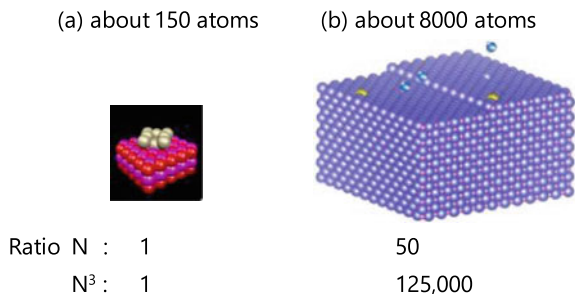
that the desorption with a large activation energy barrier is dominant at high temperatures, leading to faster desorption at temperatures higher than 187 K as shown in Fig. 8.10, in good agreement with the experimental results. Our study demonstrates the importance of kinetic theory along with accurate energetics to a more accurate and precise description of catalytic reactions.

8.4.5 Large-Scale DFT Calculations

The applicability of the first-principles DFT method for complex structures and reactions with multi-scale simulation techniques was demonstrated in the previous section. Meanwhile, there have been extensive efforts to make first-principles calculations themselves more efficient so that larger systems can be handled at higher speeds. Large-scale DFT calculations enable us to investigate precisely the energetics and electronic structures of complex systems.

As mentioned in Sect. 8.1, the computational cost of DFT calculations increases dramatically with the number of atoms N in the system (i.e., with the number of electrons and basis functions in the system), on the order of N^2 and N^3 for

Fig. 8.11 Surface structure models with approximately **a** 150 and **b** 8000 atoms



memory and computation time. For example, if the number of atoms in the system increases by a factor of 50, the computation time formally increases by a factor of 125,000 (Fig. 8.11). Owing to this rapid increase in computational cost, DFT calculations cannot handle large systems. Although depending on the amount of available computer resources, it is usually difficult to perform DFT calculations on systems with more than 1000 atoms. Even with recent advances in computing power, most DFT calculations still target systems with 500 or fewer atoms.

Even with the above size limitation, as we have seen in the previous sections, meaningful analysis is possible if the problem can be adequately represented by local structures. Meanwhile, there are many problems that cannot be adequately represented with a small structural model, such as those of nanoscale structures with large defects (such as dislocations); co-dopants; and composite defects, interfaces, and large non-periodic structures (such as amorphous materials and biomolecules). Many hyperordered structures, which are the subject of this book, are also included in these large-scale problems. Even in the case of a single dopant or single defect, a large-scale structure model is required to reproduce a situation in which the concentration is as low as in the actual situation (Fig. 8.11b).

In overcoming the size limitation, large-scale DFT calculation methods have been proposed to handle large-scale structure models with several thousand atoms or more. Table 8.3 lists large-scale DFT calculation programs.

Table 8.3 Large-scale DFT calculation software and websites

software	website (accessed Jan 2023)
BigDFT	https://bigdft.org/
CONQUEST	http://order-n.org/
CP2K	https://www.cp2k.org/
ErgoSCF	http://www.ergoscf.org/
ONETEP	https://onetep.org/
OpenMX	https://www.openmx-square.org/
PARSEC	https://parsec.odin.utexas.edu/
RSDFT	https://www.rsdf.jp/
SIESTA	https://siesta-project.org/siesta/

There are three important considerations in making large-scale DFT calculations: (1) the function used to represent the wave function and electron density, (2) how the KS equation is to be solved, and (3) the parallelization efficiency of the program. The three factors are briefly explained below, focusing on CONQUEST [42, 43], a large-scale DFT calculation program developed by the authors.

For (1), in Sect. 8.1, it was mentioned that AO basis functions and plane-wave basis functions are used to represent wave functions in conventional first-principles calculations. The locality of basis functions is an important factor in improving computational efficiency, with local functions such as AO basis functions being more suitable than plane-wave basis functions for large-scale calculations. Gaussian-type AO basis functions, which are widely used in calculations for molecules, have distributions with long tails, and the Gaussian functions of an atom would thus overlap with those of another atom at long range; i.e., the calculation of the matrix product of two atoms cannot be truncated easily. Meanwhile, the pseudo atomic orbital (PAO) basis functions, which are used in large-scale DFT codes such as CONQUEST [44], SIESTA [45, 46], and OpenMX [47, 48], are designed to be exactly zero at some distance. Core electrons are represented by a pseudopotential, and the PAOs thus represent only valence electrons (so that the functions are called pseudo AO functions). This locality of the PAOs results in the overlap matrix of the electronic Hamiltonian and basis function being sparse. This sparsity enables us to dramatically reduce the computational cost. Similar to the case for conventional AO basis functions, multiple PAOs are often used to improve accuracy. In the multi-site method [49–51] that was introduced recently in CONQUEST, local functions that describe the density matrix are constructed as linear combinations of the PAOs on the target atom together with the PAOs of neighboring atoms:

$$\phi_{i\alpha} = \sum_{\text{atom } k}^{\text{neighbors of atom } i} \sum_{\text{PAO } \mu \in k} c_{i\alpha, k\mu} \chi_{k\mu}, \quad (8.21)$$

where the α th multi-site function of atom i , $\phi_{i\alpha}$, is given as the linear combination of the PAOs (χ with index μ) belonging to atom k , which is a neighboring atom of atom i within a cutoff range. c is the linear combination coefficient. The use of the multi-site method dramatically reduces the computational cost while maintaining the accuracy of the original multiple PAO functions. Using the multi-site method, large-scale DFT calculations of several thousand to 10,000 atoms are possible even using conventional $O(N^3)$ calculation methods, such as exact diagonalization. Figure 8.12 shows an example of graphene on a Rh surface comprising approximately 3000 atoms, where the multi-site method results in acceleration by a factor of 18 [52].

For (2), in conventional DFT calculations, the electron density is optimized by solving the eigenvalue problem in the KS equation in Eq. (8.15) through exact diagonalization. The computational cost of the diagonalization is in the cubic scaling with respect to the number of atoms N ; i.e., $O(N^3)$. A method that reduces the computational cost to a linear cost with respect to N is called a linear-scaling or order- N ($O(N)$) method (Fig. 8.13).

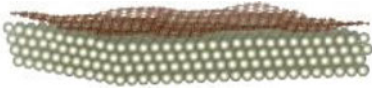
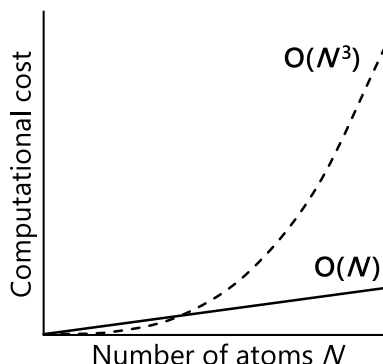
Graphene on Rh (111) surface	Computational time [sec] per SCF step	
	Primitive DZP PAO	37803.5
	Multi-site method	2156.3
3088 atoms	(with 108 MPI processes)	

Fig. 8.12 Reduction in the computational time using the multi-site method. Reproduced with permission from Ref. [52]

Fig. 8.13 Linear ($O(N)$) and cubic ($O(N^3)$) scaling with respect to the number of atoms N



A typical $O(N)$ method is to divide a large system into small subsystems, perform diagonalization calculations for each subsystem, and combine the results for the whole system; e.g., the divide-and-conquer method [53–55] or the fragment molecular orbital method [56]. The calculation accuracy of such a method depends on how appropriately the system is divided and subsystem results are combined. The density matrix minimization method used in CONQUEST and ONETEP [57] is a type of $O(N)$ method in which the density matrix (i.e., electron density) is optimized by calculating the energy derivative with respect to the density matrix:

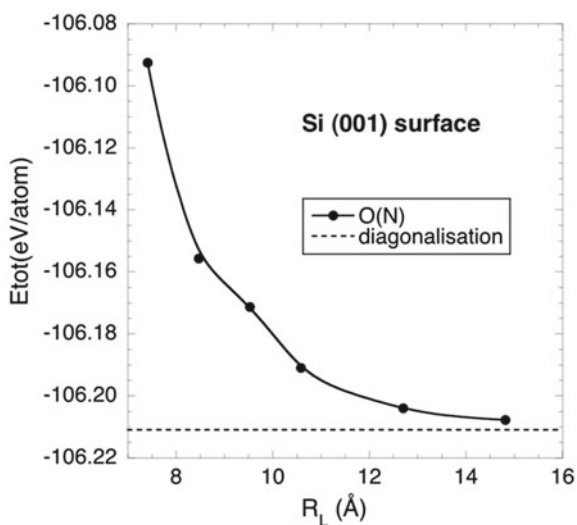
$$\frac{\partial E}{\partial \mathbf{L}} = 6(\mathbf{SLH} - \mathbf{HLS}) - 4(\mathbf{SLSLH} + \mathbf{SLHLS} + \mathbf{HLSLS}), \quad (8.22)$$

where \mathbf{H} is the KS Hamiltonian and \mathbf{S} is the overlap matrix of the local functions. \mathbf{L} is called the auxiliary density matrix and is related to the density matrix \mathbf{K} by

$$\mathbf{K} = 3\mathbf{LSL} - 2\mathbf{LSLSL}. \quad (8.23)$$

The condition in Eq. (8.23) helps maintain the power equality of the density matrix. \mathbf{H} and \mathbf{S} are sparse matrices owing to the use of local orbital functions as explained above. \mathbf{L} is made sparse by introducing an artificial spatial cutoff, and the expression in Eq. (8.22) can then be calculated as a sparse matrix product. The introduction of the cutoff for the density matrix is based on the idea of “near-sightedness,” [58]

Fig. 8.14 Cutoff dependence of the total energy calculated using the $O(N)$ method for the Si(001) surface. The energy calculated by exact diagonalization is also shown for comparison. Reproduced with permission from Ref. [59]



which means that electrons are hardly affected by distant electrons. The accuracy of the calculation depends on the cutoff, and as shown in Fig. 8.14, the result of the $O(N)$ calculation approaches that of the exact diagonalization as the cutoff range increases.

In the density matrix minimization method, the density matrix is optimized without performing diagonalization. Therefore, the KS orbitals, which correspond to eigenstates of the KS equation and are important for analyzing various physical properties, are not obtained. Large systems that require an $O(N)$ method cannot be treated using the conventional diagonalization method, and we thus need another method to obtain the eigenstates. In Ref. [60], after optimizing the density matrix, one-shot eigenstate calculation was performed using the Sakurai–Sugiura (SS) method [61]. The SS method is a sparse-matrix interior eigenproblem solver that can calculate eigenstates in given energy regions with high parallel-computing efficiency. This method is useful in practical applications, which mostly require information of the KS orbitals only in some finite energy range of interest and not the whole range. Figure 8.15 shows the results of the highest occupied molecular orbital (HOMO) and lowest unoccupied molecular orbital (LUMO) for KS orbitals of DNA in H_2O , where only the eigenstates around the HOMO–LUMO gap were calculated using the SS method.

For (3), high parallelization efficiency is crucial to large-scale calculations. Even with an $O(N)$ method, large-scale calculations are difficult to perform on a personal laptop computer and require a parallel calculation environment using a supercomputer or a medium-scale cluster system. Therefore, it is important to design the program appropriately so that not only the calculation algorithm but also the data distribution and communication during the actual execution of the calculation are of order N [62]. Figure 8.16 shows the parallelization efficiency of a large-scale DFT

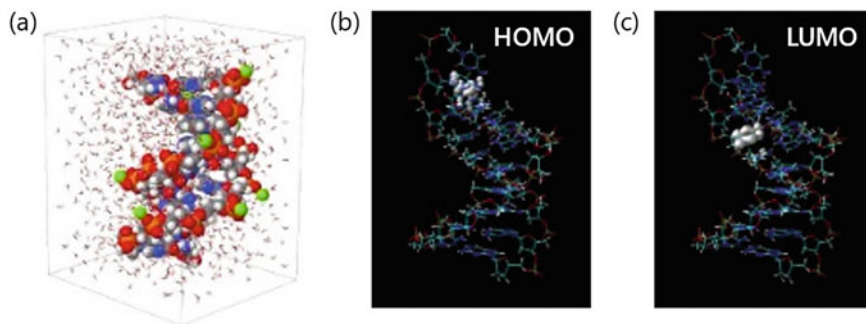


Fig. 8.15 Structure model of hydrated DNA and the HOMO and LUMO calculated using the Sakurai–Sugiura method. Reproduced with permission from Ref. [60]

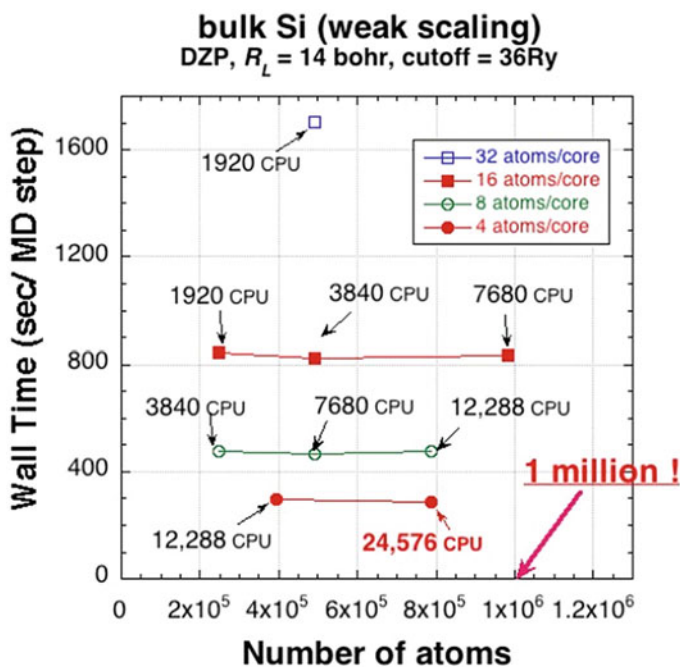
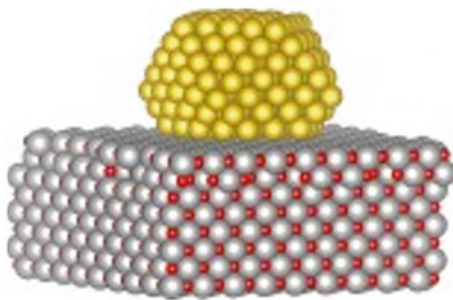


Fig. 8.16 Weak-scaling parallel efficiency of CONQUEST. The wall clock time for calculating the density matrix and atomic forces of crystalline Si using the K computer is presented. Reproduced from Ref. [63]

calculation using the K computer, a supercomputer in Japan. In Fig. 8.16, an order- N DFT calculation of a million atoms has been achieved [63].

Large-scale DFT calculations have been applied to materials with hyperordered structures, such as the supported metal nanoparticle catalysts described in Chap. 19.

Fig. 8.17 Structure of Au nanoparticles on a MgO(100) surface optimized using the multi-site method. Reproduced from Ref. [51]. CC-BY 4.0



Conventionally, calculations of metal “cluster” catalysts rather than metal “nanoparticle” catalysts on the surfaces of support bases have been widely performed, one of the reasons being the high computational cost of the conventional DFT calculation method. Calculations approximating nanoparticles with a continuum model under a periodic boundary condition have also been performed. Structural models of several thousand atoms are required to model the structure of nanoparticles of a few nanometers supported on a surface, for which large-scale DFT calculation methods are needed. Recently, structural optimizations and electronic structure analyses of Au nanoparticles having a diameter of 2 nm on a MgO support base comprising approximately 3000 atoms have been performed using the multi-site methods (Fig. 8.17) [51].

Large-scale DFT calculations have also been made for complex interfaces [64]. One example is YGaO_3 , which has a characteristic interface structure where six domains converge at a single point (i.e., a vortex core), as shown in an experimental image in Ref. [65]. A large-scale structural model is required to represent the complex interface structure. If the six domains are just aligned as shown in Fig. 8.18a, the interface can be expressed by a structural model with a few hundred atoms. However, to represent the vortex structure while maintaining symmetry under a periodic boundary condition, a structural model containing several thousand atoms is necessary as shown in Fig. 8.18b. Figure 8.18b shows the optimized structures and the electron distribution in the energy region around the bottom of the conduction band (CBM) calculated using the multi-site method. As shown in the figure, electrons are distributed more around the vortex core with $P3c1$ symmetry in the CBM energy region (Fig. 8.18b inset).

There is an example of the $O(N)$ calculation applied to Ge/Si core-shell nanowires (Fig. 8.19a) [66]. The Ge/Si core-shell nanowire is expected to be a next-generation semiconductor owing to its high integration potential and low leakage. In the case of p-type semiconductors, it is considered that the separation of the electronic states of the Si shell part, where dopants are introduced, and the Ge core part, where hole carrier current flows, reduces the leakage of electron flow owing to dopant resistance. To investigate the electronic structure of the nanowire, it is important to make both the core and shell parts thick enough as for actual materials. Therefore, the $O(N)$ method has been applied to optimize the geometry of the nanowire, including the

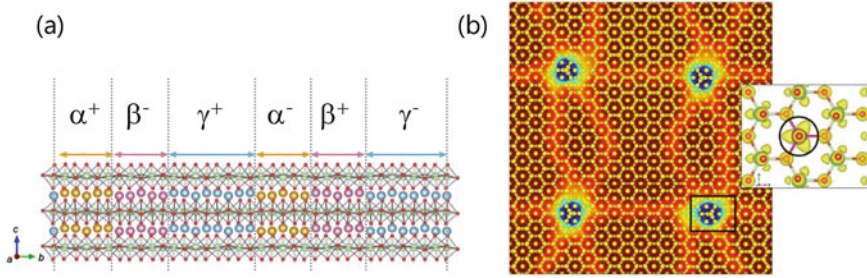


Fig. 8.18 Structures of YGaO_3 with a stripe domain pattern **a** and domain patterns with two vortex/antivortex pairs **b**. The electron distribution in the energy region from the bottom of the conduction band (ϵ_{CBM}) to ($\epsilon_{\text{CBM}} + 1 \text{ eV}$) calculated by CONQUEST is shown in the inset. Reproduced with permission from Ref. [64]

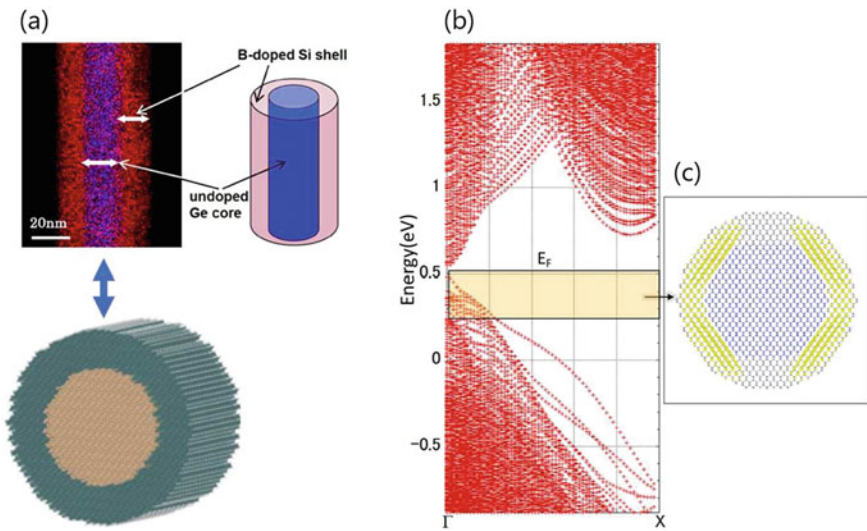


Fig. 8.19 Ge/Si core-shell nanowire and its band structure **b** and the electron distribution in the energy region from the top of the valence band (ϵ_{VBM}) to $\text{VBM} - 0.25 \text{ eV}$ **c** calculated by CONQUEST and using the Sakurai-Sugiura method. Reproduced with permission from Ref. [66]

optimization of the interface structure between Si and Ge, and the SS method has then been used to obtain the KS states around the Fermi level [66]. The calculated KS band energies and the electron distribution in the energy region around the top of the valence band (VBM) are shown in Fig. 8.19b and c. The electron distribution of the VBM is localized only in the Ge region, which supports the design concept of the nanowire; i.e., the separation of the electronic structures of the dopant site and the carrier site within a single material.

Large-scale calculations can also be applied to amorphous materials. It is often said that structural models comprising several thousand atoms are desirable for reproducing amorphous structures observed experimentally, such as by X-ray diffraction. Topological analysis and machine learning have been applied to distinguish the characteristic features of such large and complex structures, as explained in detail in Chaps. 11 and 12. There is an example in which amorphous structures have been made through large-scale DFT and analyzed by machine learning [67]. First, solids, liquids, and amorphous structures of silicon comprising approximately a thousand atoms each were created by first-principles molecular dynamics simulations with CONQUEST. The TS-LPP dimension reduction method [67] was then used to distinguish solids, liquids, and amorphous structures clearly. The method can also be used to find where a new structure corresponds to in the already-learned dimension-reduced space, which enables analysis of the time evolution of the local structure in large and complex materials (e.g., the process of a structural change from liquid to amorphous according to the annealing temperature). Such machine learning analysis is expected to be effective in analyzing characteristic local structures in hyperordered structures and their dynamics.

Acknowledgements The authors greatly appreciate the valuable suggestions and assistance given by Dr. Tsuyoshi Miyazaki (NIMS) and Dr. Jianbo Lin (NIMS) in completing this section. This work was partly supported by Grants-in-Aid for Transformative Research Areas (A) “Hyper-Ordered Structure Science” (Grant Numbers 20H05878 and JP20H05883), and for Scientific Research (B) (Grant Number JP20H02569).

References

1. Szabo A, Ostlund NS (1989) *In modern quantum chemistry: introduction to advanced electronic structure theory*. Dover Publications, New York
2. Parr R, Yang W (1989) *In Density-Functional theory of atoms and molecules*, edited by Breslow R, Goodenough JB, Halpern J, Rowlinson JS (Oxford University Press, New York)
3. Martin RM (2004) *In electronic Structure—Basic theory and practical methods*. Cambridge University Press, Cambridge
4. Kohn W, Sham LJ (1965) *Phys Rev A* 140:1133
5. Hohenberg P, Kohn W (1964) *Phys Rev B* 136:864
6. Levy M (1979) *Proc Natl Acad Sci USA* 76:6062
7. Perdew JP, Burke K, Ernzerhof M (1996) *Phys Rev Lett* 77:3865
8. Perdew JP, Ruzsinszky A, Csonka GI, Vydrov OA, Scuseria GE, Constantin LA, Zhou X, Burke K (2008) *Phys Rev Lett* 100:136406
9. Tao J, Perdew JP, Staroverov VN, Scuseria GE (2003) *Phys Rev Lett* 91:146401
10. Zhao Y, Truhlar DG (2006) *J Chem Phys* 125:194101
11. Sun J, Ruzsinszky A, Perdew JP (2015) *Phys Rev Lett* 115:036402
12. Becke AD (1993) *J Chem Phys* 98:5648
13. Heyd J, Scuseria GE, Ernzerhof M (2006) *J Chem Phys* 124:219906
14. Iikura H, Tsuneda T, Yanai T, Hirao K (2001) *J Chem Phys* 115:3540
15. Yanai T, Tew D, Handy N (2004) *Chem Phys Lett* 393:51
16. Dion M, Rydberg H, Schröder E, Langreth DC, Lundqvist BI (2004) *Phys Rev Lett* 92:246401
17. Lee K, Murray ED, Kong L, Lundqvist BI, Langreth DC (2010) *Phys Rev B* 82:081101(R)

18. Grimme S, Hansen A, Brandenburg JG, Bann C (2016) *Chem Rev* 116:5105
19. Hamada I, Otani M (2010) *Phys Rev B* 82:153412
20. Perdew JP, Ruzsinszky A, Tao J (2005) *J Chem Phys* 123:062201
21. Takano Y, Kobayashi N, Morikawa Y (2018) *J Phys Soc Jpn* 87:061013
22. Tsutsui K, Morikawa Y (2020) *Jpn J Appl Phys* 59:010503
23. Tsutsui K, Matsushita T, Natori K, Muro T, Morikawa Y, Hoshii T, Kakushima K, Wakabayashi H, Hayashi K, Matsui F, Kinoshita T (2017) *Nano Lett* 17:7533
24. Halim HH, Morikawa Y (2022) *ACS Physical Chemistry Au* 2:430
25. Vandermause J, Torrisi SB, Batzner S, Xie Y, Sun L, Kolpak AM, Kozinsky B (2020) *Npj Comput Mater* 6:20
26. Halim HH, Putra SEM, Muttaqien F, Hamada I, Inagaki K, Hamamoto Y, Morikawa Y (2021) *ACS Omega* 6:5183
27. Giesen-Seibert M, Jentjens R, Poensgen M, Ibach H (1993) *Phys Rev Lett* 71:3521
28. Stoltze P (1994) *J Phys Condens Matter* 6:9495
29. Giesen M, Schulze Icking-Konert G, Ibach H (1998) *Phys. Rev. Lett.* 80, 552
30. Giesen M (2001) *Prog Surf Sci* 68:1
31. Giesen M, Ibach H (2003) *Surf Sci* 529:135
32. Marinica M-C, Barreateau C, Spanjaard D, Desjonquères M-C (2005) *Phys Rev B* 72:115402
33. Nielsen J, d' Avezac M, Hetherington J, Stamatakis M (2013) *J Chem Phys* 139:224706
34. Putra SEM, Muttaqien F, Hamamoto Y, Inagaki K, Hamada I, Morikawa Y (2019) *J. Chem. Phys.* 150, 154707
35. Fujitani T, Choi Y, Sano M, Kushida Y, Nakamura J (2000) *J Phys Chem B* 104:1235
36. Nakano H, Nakamura I, Fujitani T, Nakamura J (2001) *J Phys Chem B* 105:1355
37. Baber AE, Mudiyansele K, Senanayake SD, Beatriz-Vidal A, Luck KA, Sykes ECH, Liu P, Rodriguez JA, Stacchiola DJ (2013) *Phys Chem Chem Phys* 15:12291
38. Marcinkowski MD, Murphy CJ, Liriano ML, Wasio NA, Lucci FR, Sykes ECH (2015) *ACS Catal* 5:7371
39. Shiozawa Y, Koitaya T, Mukai K, Yoshimoto S, Yoshinobu J (2015) *J Chem Phys* 143:234707
40. Shiozawa Y, Koitaya T, Mukai K, Yoshimoto S, Yoshinobu J (2020) *J Chem Phys* 152, 044703
41. Shiotari A, Putra SEM, Shiozawa Y, Hamamoto Y, Inagaki K, Morikawa Y, Sugimoto Y, Yoshinobu J, Hamada I (2021) *Small* 17:200810
42. Hernandez E, Gillan MJ, Goringe CM (1996) *Phys Rev B* 53:7147
43. Nakata A, Baker JS, Mujahed SY, Poulton JTL, Arapan S, Lin J, Raza Z, Yadav S, Truffandier L, Miyazaki T, Bowler DR (2020) *J Chem Physics* 152:164112
44. Bowler DR, Baker JS, Poulton JTL, Mujahed SY, Lin J, Yadav S, Raza Z, Miyazaki T (2019) *Jpn J Appl Phys* 58:100503
45. García A, Papior N, Akhtar A, Artacho E, Blum V, Bosoni E, Brandimarte P, Brandbyge M, Cerdá JI, Corsetti F, Cuadrado R, Dikan V, Ferrer J, Gale J, García-Fernández P, García-Suárez VM, García S, Huhs G, Illera S, Korytár R, Koval P, Lebedeva I, Lin L, López-Tarifa P, Mayo SG, Mohr S, Ordejón P, Postnikov A, Pouillon Y, Pruneda M, Robles R, Sánchez-Portal D, Soler JM, Ullah R, Yu VW-z, Junquera J (2020) *J. Chem. Phys.* 152, 204108
46. Anglada E, Soler JM, Junquera J, Artacho E (2002) *Phys Rev B* 66:205101
47. Ozaki T (2003) *Phys Rev B* 67:155108
48. Ozaki T, Kino H (2004) *Phys Rev B* 69, 195113
49. Nakata A, Bowler DR, Miyazaki T (2014) *J Chem Theory Comput* 10:4813
50. Nakata A, Bowler DR, Miyazaki T (2015) *Phys Chem Chem Phys* 17:31427
51. Nakata A, Bowler DR, Miyazaki T (2022) *J Phys Soc Jpn* 91:091011
52. Romero-Muñiz C, Nakata A, Pou P, Bowler DR, Miyazaki T, Pérez R (2018) *J Phys: Condens Matter* 30:505901
53. Yang W (1991) *Phys Rev Lett* 66:1438
54. Yang W (1991) *Phys Rev A* 44:7823
55. Yang W (1992) *J Mol Struct: THEOCHEM* 255:461
56. Kitaura K, Ikeo E, Asada T, Nakano T, Uebayasi M (1999) *Chem Phys Lett* 313:701

57. Prentice JCA, Aarons J, Womack JC, Allen AEA, Andrinopoulos L, Anton L, Bell RA, Bhandari A, Bramley GA, Charlton RJ, Clements RJ, Cole DJ, Constantinescu G, Corsetti F, Dubois SM-M, Duff KKB, Escartín JM, Greco A, Hill Q, Lee LP, Linscott E, O'Regan DD, Phipps MJS, Ratcliff LE, Ruiz Serrano Á, Tait EW, Teobaldi G, Vitale V, Yeung N, Zuehlsdorff TJ, Dziedzic J, Haynes PD, Hine NDM, Mostofi AA, Payne MC, Skylaris C-K (2020) *J Chem Phys* 152, 174111
58. Prodan E, Kohn W (2005) *PNAS* 102:11635
59. Miyazaki T, Nakata A, Bowler DR (2022) In *System-Materials Nanoarchitectonics*, edited by Wakayama Y, Ariga K, pp 303–317 (Springer Japan KK, Tokyo)
60. Nakata A, Futamura Y, Sakurai T, Bowler DR, Miyazaki T (2017) *J Chem Theory Comput* 13:4146
61. Sakurai T, Sugiura H (2003) *J Comput Appl Math* 159:119
62. Bowler DR, Miyazaki T, Gillan MJ (2001) *Comput Phys Commun* 137:255
63. Arita M, Arapan S, Bowler DR, Miyazaki T (2014) *J Adv Simulation Sci Eng* 1:87
64. Småbråten DR, Nakata A, Meier D, Miyazaki T, Selbach SM (2020) *Phys Rev B* 102:144103
65. Kumagai Y, Spaldin NA (2013) *Nat Commun* 4:1540
66. Miyazaki T (2018) *ECS Trans* 86:269
67. Tamura R, Matsuda M, Lin J, Futamura Y, Sakurai T, Miyazaki T (2022) *Phys Rev B* 105:075107